Terahertz Magnetic Mirror Realized with Dielectric Resonator Antennas

Daniel Headland, Shruti Nirantar, Withawat Withayachumnankul, Philipp Gutruf, Derek Abbott, Madhu Bhaskaran, Christophe Fumeaux, and Sharath Sriram**

An array of highly efficient terahertz passive dielectric resonator antennas (DRAs) is investigated. The realization of this device requires relatively thick, single-crystal silicon to be incorporated on a metal film. To this end, an unconventional microfabrication procedure is developed, which makes use of a combination of SU-8-assisted bonding, photolithography, and deep reactive ion etching. The fabricated DRAs exhibit a magnetic dipole mode of resonance, and hence the device behaves as a magnetic mirror, with a 30% useful bandwidth. The efficiency of the DRA array is determined by numerical simulation to be 97% on resonance at 0.8 THz. This experimental demonstration of DRAs at terahertz frequencies opens opportunities for highly efficient terahertz components with impact in the areas of imaging, sensing, and communications.

Essentially, an electromagnetic wave reflected from a perfect electrical conductor (PEC) experiences a 180° phase shift in its electric field component. Owing to this phase shift, the standing wave that is produced from the interference between the incident and reflected waves results in zero absolute electric field strength at the PEC surface. A consequence of this process is that strong field–matter interaction can only occur at a minimum distance away from a PEC surface. As a counterpart of a PEC, a perfect magnetic conductor (PMC) imposes a zero phase change on the electric component of the reflected wave, and the magnetic component undergoes phase reversal. In this case, the incident and reflected electric fields close to the surface of a PMC are in phase. Hence, the surface of the PMC is at a local maximum of absolute electric field strength. An object placed close (<< $\lambda/4$) to the surface of a PMC will therefore have a stronger interaction with electric fields than an object placed close to the surface of a PEC. This unique PMC property can be exploited in a broad range of applications from antennas,[1–4] sensing platforms,[5] to optical components.

Magnetic conductors do not naturally occur, but their response can be approximated using structured surfaces, termed artificial magnetic conductors (AMCs), or magnetic mirrors.[6–8] Such a response is typically achieved with arrays of resonant elements, such as metallic resonators supported by a dielectric layer and a ground plane.[8–11] Each resonator, together with the ground plane, forms a magnetic dipole that exhibits magnetic phase reversal near resonance. Thus, AMCs mimic the response of a PMC within a certain operational bandwidth, with near-unity reflectivity and a near-zero phase change of the electric field upon reflection. Metallic resonators are well covered in the microwave range, as they form the basis for conventional reflectarrays.[12–18] They remain an active field of research in the terahertz[19–23] and optical frequency ranges,[24–26] but are increasingly lossy at such frequencies, given the non-negligible loss of the Drude metals. At terahertz frequencies, there is an additional challenge of identifying low-loss dielectrics suitable to support the metallic resonators.[27] To bypass ohmic heat dissipation, resonant dielectric structures are preferable for functional and efficient AMCs at terahertz and optical frequencies.[28–30]

Inside a dielectric structure of moderate to high relative permittivity, electromagnetic radiation is confined into standing waves, or resonant modes. The resonance frequency is dependent on the geometry and material properties of the dielectric resonator (DR). If the DR is unshielded, the modes can couple with free space radiation,[31] and if the DR is utilized as a radiator in this way, it can be termed a dielectric resonator antenna (DRA).[32,33] DRAs are theoretically scalable across a broad range of frequencies,[34] and have been demonstrated in the visible range.[35] Key to the operation of the DRA is the quality factors: Q_{diss} is associated with energy lost to dissipation and Q_{rad} is associated with energy radiated to free space. In the majority of cases, it is beneficial for a DRA to have high Q_{diss} in order to ensure efficient operation, and hence low-loss dielectrics are sought to construct DRAs. However, the choice of Q_{rad} depends on the desired application. High Q_{rad} is generally beneficial for sensing applications, in order to maximize resonator sensitivity. Such high Q_{rad} DRAs, using a dielectric of high relative permittivity, have previously been employed in the terahertz range as resonators for a metamaterial application.[36] However, a drawback of high Q_{rad} is narrowband operation.

D. Headland, Dr. W. Withayachumnankul, Prof. D. Abbott, Prof. C. Fumeaux
School of Electrical & Electronic Engineering
The University of Adelaide
Adelaide, South Australia 5005, Australia
E-mail: cfumeaux@eleceng.adelaide.edu.au

S. Nirantar, Dr. W. Withayachumnankul, P. Gutruf, Dr. M. Bhaskaran, Dr. S. Sriram
Functional Materials and Microsystems Research Group
School of Electrical and Computer Engineering
RMIT University
Melbourne, Victoria 3000, Australia
E-mail: sharath.sriram@gmail.com

S. Nirantar, P. Gutruf, Dr. M. Bhaskaran, Dr. S. Sriram
Micro Nano Research Facility
RMIT University
Melbourne, Victoria 3000, Australia

Dr. W. Withayachumnankul
Interdisciplinary Graduate School of Science and Engineering
Tokyo Institute of Technology
Ookayama 152-8552, Meguro-ku, Tokyo, Japan

DOI: 10.1002/adma.201503069

Reducing Q_{rad} of the DRAs by selecting a moderate-permittivity dielectric material will enhance bandwidth, improving suitability for communications and beam control applications.

With regard to the dielectric material, single-crystal silicon has moderate relative permittivity and exceptionally low dissipation loss, suitable for terahertz DRA applications with high Q_{diss} and moderate Q_{rad}. While single-crystal silicon is abundantly available in the form of wafers, it cannot be grown on metal-coated substrates or on oxide/amorphous substrates. This restriction has limited the exploration of single-crystal silicon microstructure applications.

In this work, we demonstrate a uniform array of passive terahertz DRAs of moderate quality factor. The DRA-based array is designed to function as a terahertz AMC of moderate bandwidth, with zero reflection phase. We also present a brief numerical study that compares the efficiency of the DRA with that of a conventional metallic resonator of similar resonance characteristics. This experimental realization of the terahertz DRA array demonstrates new fabrication techniques for combining single-crystal silicon with metallic or amorphous substrates. Furthermore, this realization of a terahertz DRA has significant implications for terahertz science and technology, as it provides a much needed high-efficiency alternative to metallic resonators. Given that power available from typical terahertz sources is limited, efficiency is a key concern. The applicability of this work is therefore not limited to the present AMC application, but rather can be applied to virtually any functionality previously realized by metallic resonators.

As shown in **Figure 1**a, a unit cell of the DRA array is composed of a cylinder of single-crystal high-resistivity float-zone intrinsic silicon (HR Si) on a gold ground plane. The HR Si is chosen due to its moderate relative permittivity ($\varepsilon_r = 11.68$), and exceptionally low dielectric loss ($\tan\delta < 4 \times 10^{-5}$) in the terahertz range.[37] The cylindrical shape is chosen due to isotropic response and practical fabrication concerns. The dimensions of the passive DRA are optimized for resonance at 0.8 THz. The thickness of the gold layer is 200 nm, which is well above the skin depth in the relevant frequency range (≈90 nm at 0.8 THz). Given that the lattice constant at the resonance frequency is equal to 0.4λ, there are no array diffraction effects associated with this device, as grating lobes require a lattice constant that is $\geq\lambda$. Numerical modeling, using the Drude model to account for realistic dielectric and metallic losses, is utilized in order to investigate the field–matter interaction and resonance of the structure in detail. The field plot in Figure 1b shows the fundamental hybrid mode (commonly denoted as $HEM_{11\delta}$, or magnetic dipole mode) in a single DRA element, excited by a normally incident plane wave. In order to operate as an AMC, the uniform DRA array must exhibit low loss, and impart a zero phase shift on the electric field of an incident wave, within a given range of operation. According to the response given in Figure 1c, the simulated peak loss of the DRA is 0.13 dB, equivalent to reflecting incident energy with 97% efficiency. Furthermore, phase zero crossing is observed at ≈0.8 THz, which is indicative of AMC response. The AMC operation is further confirmed via near field standing wave results given in Figure 1d,e. It is clear that the maxima in the field magnitude for the DRA correspond to minima for the un-patterned ground plane, as expected.

Designs requiring control over reflection phase in the terahertz range are conventionally implemented with metallic resonators, and such designs typically consist of a periodic, planar metallic structure separated from a ground plane by a polymer dielectric spacer.[19,20,22] The choice of polymers for the spacer, as opposed to lower loss materials such as ceramics or intrinsic semiconductors, is due to practical fabrication concerns; while polymers may be spin-coated into the thin dielectric layers required for terahertz metallic resonators, lower loss dielectrics are not compatible with such processes.[27] In order to compare the DRA in this work to the conventional metallic resonator approach, a circular patch-based metallic resonator antenna (MRA), illustrated in **Figure 2**a, is investigated. The circular patch resonator design in particular is selected because the isotropic nature of its response and the field orientation of its fundamental resonance mode are similar to those of the DRA. The unit cell dimensions of the MRA are identical to those of the DRA, and the spacer thickness and patch diameter are varied in order to optimize the response of the MRA.

A comparative numerical study of the response of the DRA and the MRA is given in Figure 2b. In order to ensure equivalence of resonance, the MRA is optimized to share the fundamental resonance frequency with the DRA, and to have the closest possible match to its phase response. Note that, due to differences in the nature of higher-order resonances in both resonators, the phase response of the MRA is not well matched to the DRA above the fundamental resonance of 0.8 THz. Furthermore, metallic resonators are generally sensitive to the surrounding dielectric,[38] and metal–dielectric–metal structures are typically associated with non-negligible losses. Therefore, it is unlikely that a realistic MRA's dielectric spacer could be optimized to 1 µm precision in order to match the resonance as we have done in the simulation. A range of values for the dielectric loss tangent of the polymer spacer is simulated, including a lossless case, and the selected finite values of loss tangent correspond to polypropylene (PP),[39] polyimide,[40] and polydimethylsiloxane (PDMS),[41] as these are all commonly used polymer dielectrics in the terahertz range.[21,22,42–51] It is found that, in the idealized case in which the dielectric spacer of the MRA is lossless, the DRA outperforms the MRA by a small margin of 0.17 dB. It can be inferred from this that, because the ground plane is common to both designs, and the MRA's dielectric spacer is lossless in this case, the added loss originates in ohmic dissipation in the resonant patch itself. In the case corresponding to PP, the low dielectric loss leads to the DRA outperforming the MRA by a similarly small margin of 0.3 dB. The advantage of the DRA becomes more apparent when lossier dielectrics are utilized. When the loss tangent corresponds to polyimide, the DRA outperforms the MRA by 2 dB. In the highest-loss case considered, corresponding to PDMS, the DRA outperforms the MRA by 3.7 dB. In order to gain further insight into the loss in the DRA and MRA, analysis of the individual origins of loss is given in Figure 2c,d. It is found that the majority of the loss in the DRA on resonance is in the ground plane; hence ohmic loss is exacerbated by field confinement on resonance. In the case of the MRA, the dielectric spacer corresponding to PP exhibits low loss, which is comparable to the ohmic loss in

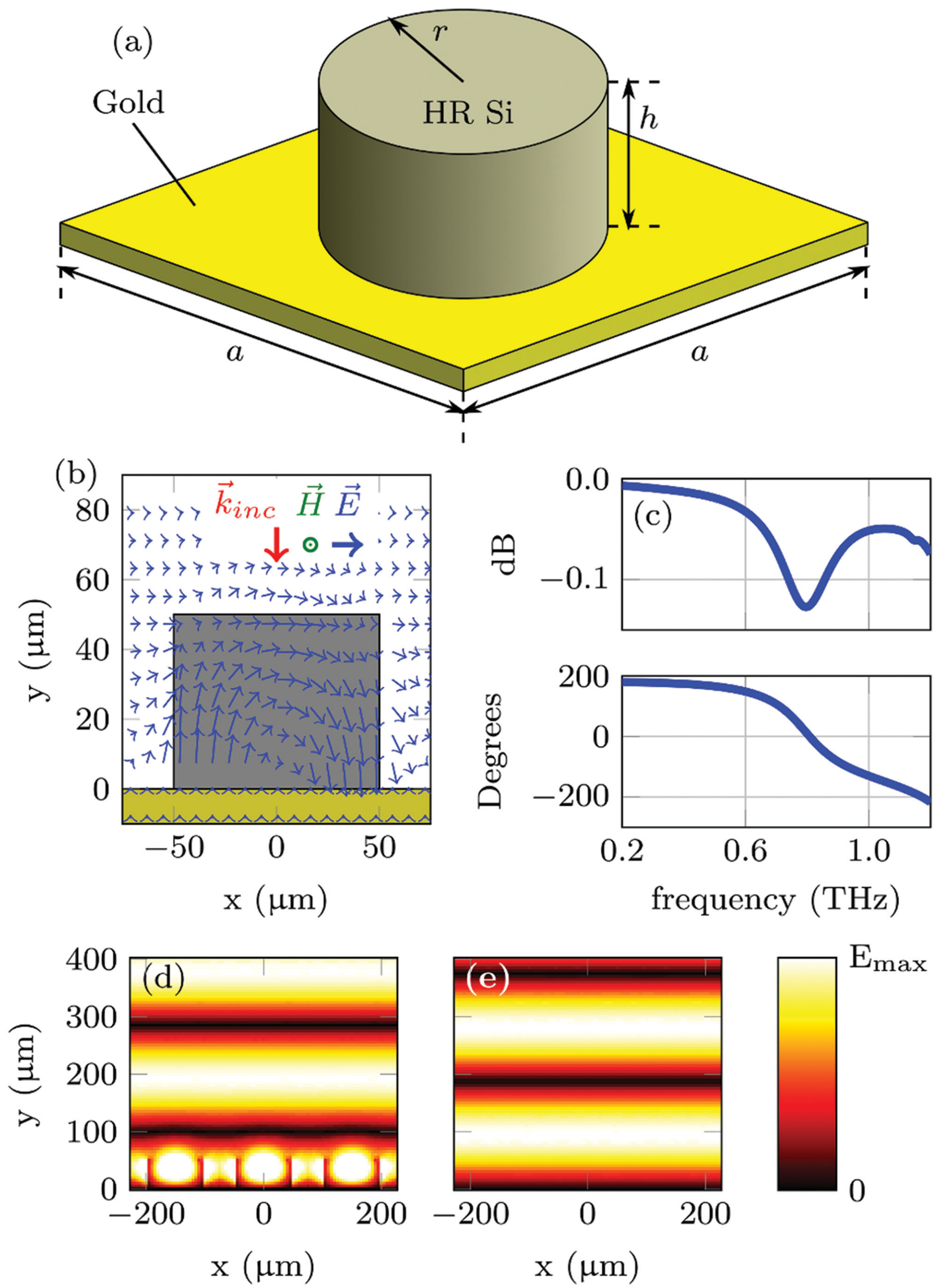

Figure 1. Single cylindrical DRA element a) schematic diagram, with a = 150 μm, r = 50 μm, and h = 50 μm, b) cross-sectional instantaneous field plot of single element in uniform array, when illuminated by normally incident plane wave, showing fundamental $HEM_{11\delta}$ mode excited in dielectric resonator, c) reflection coefficient for normally incident radiation, d) near-field standing wave pattern of DRA array, and e) near-field standing wave pattern of un-patterned gold ground plane.

the patch and ground plane. In both other cases, however, the majority of the loss on resonance is contributed by dielectric loss in the polymer spacer, which is once again exacerbated by resonance.

For reflectarray applications in particular, the question of loss is critical, as loss can diminish the phase range of a resonator.[52] Therefore, low efficiency resonators do not merely impair the performance of a reflectarray, but rather, as reflectarrays require resonators with a sufficiently broad phase range, they may compromise functionality altogether.

The proposed structure is fabricated in order to experimentally validate its performance as a terahertz AMC. In order to realize this design, a silicon–metal–polymer–silicon fabrication process was devised, utilizing microfabrication as a combination of SU-8-assisted bonding, photolithography, and plasma-enhanced deep reactive ion etching (with the Bosch silicon

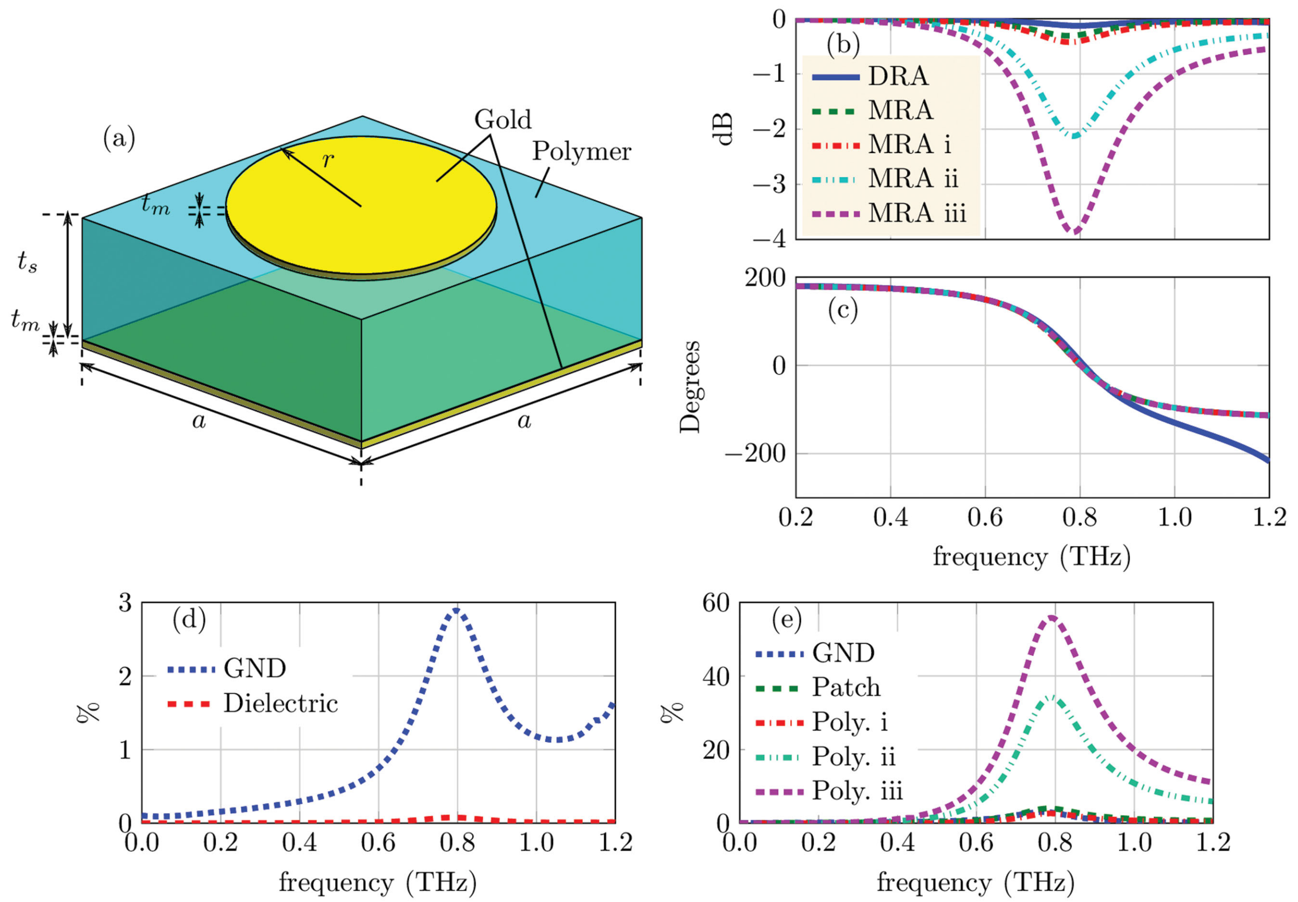

Figure 2. Comparison of the cylindrical DRA with a circular patch-based metallic resonator antenna (MRA) that is engineered to have comparable phase response. a) Simulated metallic resonator structure, with a = 150 µm, r = 59 µm, t_s = 21 µm, and t_m = 0.2 µm, and b,c) magnitude and phase responses of the DRA with the MRA, where the dielectric properties of the polymer spacer are ε_r = 2.25. Loss tangent values simulated are tanδ = 0.0, i) tanδ = 0.002, corresponding to PP,[39] ii) tanδ = 0.031, corresponding to polyimide,[40] and iii) tanδ = 0.06, corresponding to PDMS.[41] d) Analysis of individual origins of loss in the DRA, and e) analysis of individual origins of loss in the MRA.

etching process).[53–55] A schematic of the fabrication process is depicted in **Figure 3**a–f, and details are given in the Experimental Section. A diagram of the layered construction of the completed structure is given in Figure 3g, and a false color SEM image, showing cylinders of high quality is given in Figure 3h.

The reflection response of the DRA array is characterized using terahertz time-domain spectroscopy (THz-TDS), and is given in **Figure 4** (see Supporting Information). The response to normally incident radiation is given in Figure 4a,b, and close agreement with the simulated phase response is attained. The results show the zero phase crossing characteristic of a magnetic conductor occurring at ≈0.81 THz, as predicted from simulations. The useful bandwidth of the AMC, typically defined as the frequency range between +90° and –90°,[1] is about 30%, namely from 0.71 to 0.95 THz. The magnitude response appears to exceed unity around resonance, which is contrary to the slight loss in the simulated response. We attribute this to an enhancement in the effective aperture of the overall array due to mutual coupling between DRA elements (see Supporting Information).[56] This reduces the beam divergence, and therefore results in greater magnitude than the un-patterned reference mirror. This effect was not accounted for in the simulated response. Additionally, it should be noted that, given the large number of elements in the array, factors such as Mie scattering and the radar cross section of individual elements are insignificant compared to array factor and coupling effects.

The response to obliquely incident radiation at an incidence angle of 45° is given in Figure 4c–f. There is substantial variation in the magnitude response, possibly due to reductions in dynamic range imposed by the use of the iris, as described in the Experimental Section. Other possible explanations include minor alignment issues and array coupling effects. This magnitude fluctuation issue, however, does not wholly diminish confidence in the veracity of the phase response, as the phase component is less vulnerable than magnitude to noise in THz-TDS.[57,58] As with the results for normal incidence, there is a strong agreement with simulation in the phase response, and resonance at ≈0.8 THz is observed for oblique incidence in both polarizations. In the case of the TE polarization, the phase response shows the zero phase crossing at 0.78 THz, and useful bandwidth from 0.72 to 0.87 THz. In the case of the TM phase response, the simulated response shows a zero crossing at 0.78 THz, but the measured response shows the crossing at 0.8 THz. This discrepancy is potentially due to some small

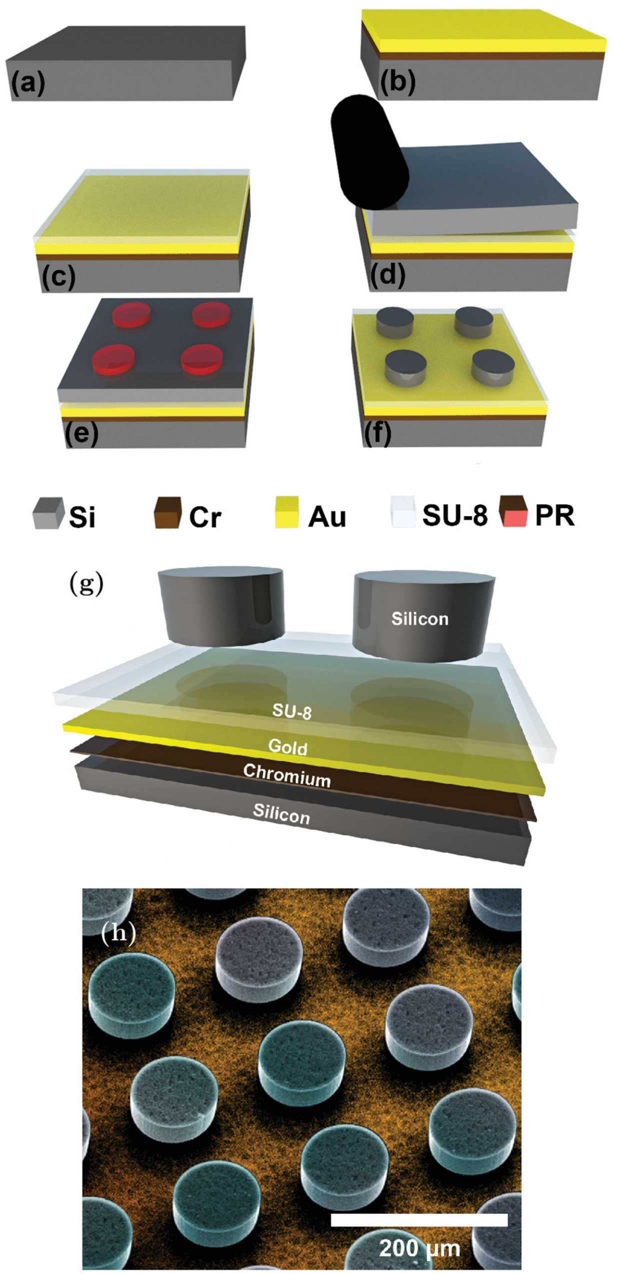

Figure 3. Experimental realization of terahertz artificial magnetic conductors a–f) fabrication process, g) layered view of complete structure, and h) false color SEM image.

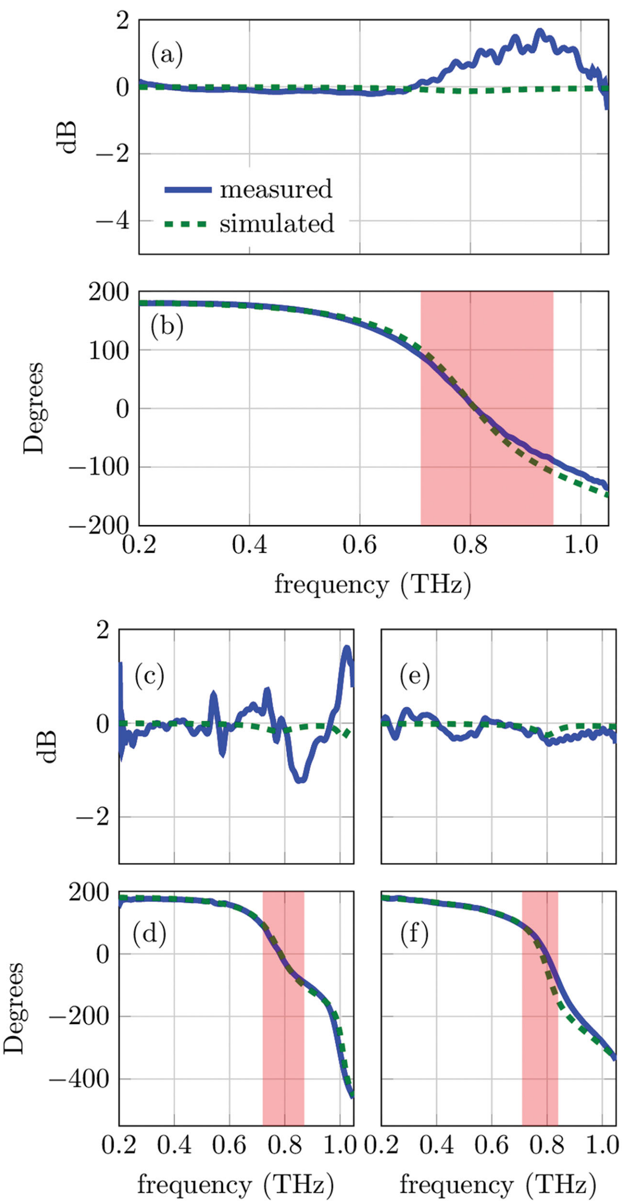

Figure 4. Reflection characteristics of the THz DRA array, showing a,b) response to normal incidence, c,d) response to oblique incidence at 45° with TE polarization, and e,f) response to oblique incidence with TM polarization. Useful bandwidth for AMC functionality is lightly shaded in red.

misalignment in the THz-TDS system. The measured useful bandwidth in the TM polarization is 0.71 to 0.84 THz. The reason for the disparity in the phase response for the normal and oblique incidences is that different higher-order modes of resonance may be lightly excited in each case, and these resonances jointly contribute to the overall phase response. The intersection of the useful ranges for all cases tested is 0.72 to 0.84 THz, and hence the common bandwidth for normal incidence and both oblique polarizations is 15%.

In conclusion, an array of passive terahertz DRAs operating at 0.8 THz has been designed, fabricated, and characterized with THz-TDS. An unconventional fabrication process was utilized to realize the etched microstructures of single-crystal silicon on metal. While being used to experimentally demonstrate a terahertz AMC, the approach is adaptable to any micro-/nanoelectronic device or process. Given the high efficiency and phase response of the DRA array, it behaves as an AMC with 30% bandwidth for normal incidence, and a tolerance to oblique excitation up to at least 45°. The demonstrated AMC is a precursor for advanced structures in terahertz antenna and sensing applications, by exploiting the electric antinode near the surface. The terahertz DRA can also be considered a high-efficiency alternative to metallic resonators in beam-shaping reflectarray applications that impart a spatially-varying phase response to the reflected waves.

Experimental Section

Numerical Modeling of DRAs: The commercially available software package CST Microwave Studio was employed for the numerical modeling of the DRAs. Floquet ports, together with unit cell boundary conditions, were employed in order to study the behavior of a single element in a uniform, infinite array of DRAs. The port was de-embedded onto the ground plane to observe the phase response. To account for the finite loss in the silicon, the Drude model was employed to model its material properties. Based on the minimum resistivity of 2 kΩ cm provided by the manufacturer, the carrier concentration was estimated to be around 2×10^{12} cm^{-3}, and the mobility to be around 1360 cm^2 V^{-1} s^{-1}. Thus the plasma frequency and relaxation time were equal to $f_p = 0.025$ THz and $\tau_c = 0.202$ ps, respectively. For the gold ground plane, given the low penetration of field into the metal, a surface impedance model was considered adequate.[34] The Drude model was also employed in order to calculate the frequency-dependent surface impedance of gold across the relevant frequency range,[59] with DC conductivity of $\sigma_{DC} = 4.1 \times 10^7$ S m^{-1}, and scattering relaxation time $\tau = 0.15$ ps.[60]

Microfabrication of Sample: A three-inch silicon wafer was cleaned with solvents and dried with compressed nitrogen (Figure 3a). A 200 nm film of gold was deposited on to the wafer, along with a 20 nm chromium adhesion layer. The two metal thin films were deposited by electron beam evaporation (PVD75, Kurt J. Lesker Co.) at a rate of 0.1 nm s^{-1} after pumping down to a base pressure of 1×10^{-7} Torr (Figure 3b). The functionality of the terahertz dielectric resonator relied on single-crystal high resistivity silicon on a metal ground plane. To achieve this, a process was undertaken that enabled bonding of single-crystal silicon to either metal-coated on non-metallic substrates using a SU-8 adhesion layer. The gold-coated silicon wafer (from Figure 3b) was spin-coated with a layer of SU-8 2000.5 at 3000 rpm to achieve a film thickness of 500 nm (Figure 3c). The SU-8 film was cross-linked using UV exposure for 10 s with 65 mJ cm^{-2} energy (Karl Süss MJB3 mask aligner). A HR Si wafer of thickness 125 µm and resistivity >5 kΩ cm was diced into 35 × 35 mm^2 sections. This HR Si section was then bonded to the SU-8 and gold-coated substrate (from Figure 3c) by passing it through a table-top laminator at 100 °C at slow speed, which cured the SU-8 while forming a strong bond to the HR Si (Figure 3d). The bonded 125 µm thin HR Si was thinned down to 50 µm in order to fabricate the required dielectric resonators. The thinning of the silicon was undertaken by plasma-enhanced deep reactive ion etching (DRIE; Oxford PlasmaPro 100 Estrelas). This etching was performed in a single step with gaseous mixture of C_4F_8 (10 sccm) and SF_6 (200 sccm) with inductively coupled plasma (ICP) power of 1500 W for 6 min. Subsequently, photolithography was performed using a thick AZ4562 photoresist (PR) spun at 2500 rpm resulting in 7.5 µm thick layer for defining patterns corresponding to the diameter of the terahertz dielectric resonators (Figure 3e). Photolithography was followed by DRIE as above, but with cyclic processing known as Bosch silicon etching. Each cycle of the etching recipe was composed of three steps: deposition, break, and etching. In the deposition step, a gaseous mixture of C_4F_8 (200 sccm) and SF_6 (10 sccm) with ICP power of 1000 W for 3 s was utilized. The break step utilized C_4F_8 (10 sccm), SF_6 (100 sccm), and ICP power of 1000 W for 2 s. The etching step comprised a gaseous mixture of C_4F_8 (10 sccm) and SF_6 (200 sccm) with ICP power of 1500 W for 3 s. With this recipe an approximate etch rate of 0.8 µm per cycle was obtained for the HR Si. The required 50 µm deep etch was achieved in 65 cycles (Figure 3f). The photoresist was stripped off and the height of pillars verified with a scanning electron microscope (Nova NanoSEM FEI Systems).

THz-TDS Characterization of Fabricated Sample: A fiber-coupled Menlo TERA K15 THz-TDS system was used to characterize the reflection response of the sample, with the experimental setup[21] shown in **Figure 5**. If a focused beam were employed to excite the resonators, it would introduce a range of angles of incidence, and would therefore be a poor approximation of the plane-wave excitation used in simulations. It was therefore deemed necessary to probe the response of the DRA array with a collimated terahertz beam. As the size of the patterned area was less than the ≈20 mm beam waist of the collimated terahertz beam, a ≈5 mm diameter iris was required to isolate the reflection from the patterned portion of the sample, at the cost of reduced dynamic range. Another consequence of clipping the beam to a ≈5 mm diameter was the introduction of diffractive effects, which resulted in increased beam divergence. This beam divergence was common to both measurements, and hence normalization was valid to remove the influence of the iris. In the case of the normally incident measurements, a polished silicon wafer was utilized as a beam splitter, and this was expected to impose further reductions on dynamic range. For the normal measurements, the setup in Figure 5a was utilized, and a peak dynamic range of 35 dB, and

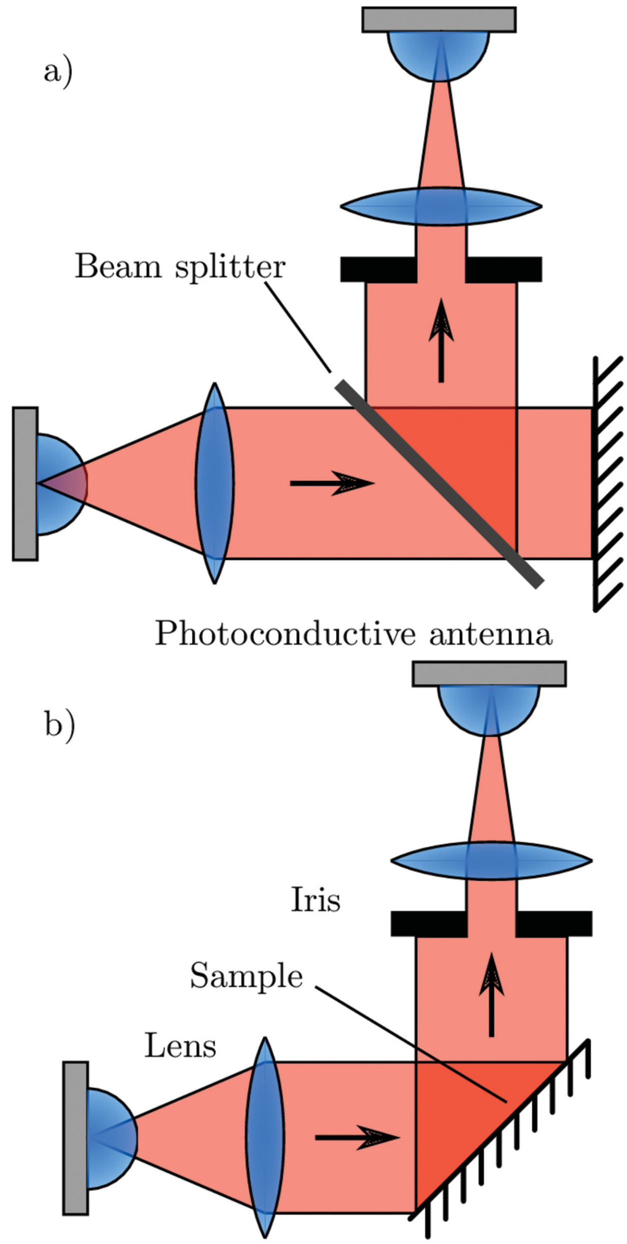

Figure 5. Measurement setup for a) measurement of normally incident radiation, and b) oblique measurement at 45° of incidence.

a bandwidth of 1.4 THz, were observed. For the oblique measurements, the setup in Figure 5b was utilized, and peak dynamic range and bandwidth were 39 dB and 1.6 THz, and 36 dB and 1.8 THz, for the TE and TM measurements, respectively. All measurements were performed in a dry-air atmosphere, using a gold mirror as a reference. The total path length in all experiments was ≈30 cm.

Supporting Information

Supporting Information is available from the Wiley Online Library or from the author.

Acknowledgements

The authors acknowledge the Australian Research Council (ARC) for infrastructure support via LE120100004 (M.B., S.S.), Charan Shah, Appu Vinod, and Prateek Mann of RMIT University for assistance with microfabrication process development, and Linnea Rundgren of Linear Imaging for micrograph coloration. D.A. and C.F. acknowledge the ARC Future Fellowship funding scheme under FT120100351 and FT100100585, respectively.

Received: June 25, 2015
Revised: August 20, 2015
Published online: October 9, 2015

[1] A. P. Feresidis, G. Goussetis, S. Wang, J. C. Vardaxoglou, *IEEE Trans. Antennas Propag.* **2005**, *53*, 209.
[2] C. Guclu, J. Sloan, S. Pan, F. Capolino, *IEEE Antennas Wireless Propag. Lett.* **2011**, *10*, 1536.
[3] A. Vallecchi, J. R. De Luis, F. Capolino, F. De Flaviis, *IEEE Trans. Antennas Propag.* **2012**, *60*, 51.
[4] M. Miri, N. Otrooshi, Y. Abdi, *J. Opt. Soc. Am. B* **2013**, *30*, 3027.
[5] S. Yagitani, T. Sunahara, T. Nakagawa, D. Hiraki, Y. Yoshimura, H. Sugiura, *Proc. URSI Int. Symp. Electromag. Theory* **2013**, 691.
[6] D. Sievenpiper, L. Zhang, R. F. Broas, N. G. Alexopolous, E. Yablonovitch, *IEEE Trans. Microwave Theory Tech.* **1999**, *47*, 2059.
[7] A. Schwanecke, V. Fedotov, V. Khardikov, S. Prosvirnin, Y. Chen, N. Zheludev, *J. Opt. A: Pure Appl. Opt.* **2007**, *9*, L1.
[8] M. Esfandyarpour, E. C. Garnett, Y. Cui, M. D. McGehee, M. L. Brongersma, *Nat. Nanotechnol.* **2014**, *9*, 542.
[9] D. J. Kern, D. H. Werner, A. Monorchio, L. Lanuzza, M. J. Wilhelm, *IEEE Trans. Antennas Propag.* **2005**, *53*, 8.
[10] M. Hiranandani, A. Yakovlev, A. Kishk, *IEE Proc. Microwaves Antennas Propag.* **2006**, *153*, 487.
[11] V. Fedotov, A. Rogacheva, N. Zheludev, P. Mladyonov, S. Prosvirnin, *Appl. Phys. Lett.* **2006**, *88*, 091119.
[12] J. Huang, *Proc. IEEE Antennas Propag. Soc. Int. Symp.* **1991**, 612.
[13] D.-C. Chang, M.-C. Huang, *Electron. Lett.* **1992**, *28*, 1489.
[14] J. Huang, R. J. Pogorzelski, *IEEE Trans. Antennas Propag.* **1998**, *46*, 650.
[15] D. Pozar, S. Targonski, R. Pokuls, *IEEE Trans. Antennas Propag.* **1999**, *47*, 1167.
[16] J. A. Encinar, J. A. Zornoza, *IEEE Trans. Antennas Propag.* **2003**, *51*, 1662.
[17] S. V. Hum, J. Perruisseau-Carrier, *IEEE Trans. Antennas Propag.* **2014**, *62*, 183.
[18] R. Florencio, J. Encinar, R. Boix, V. Losada, G. Toso, *IEEE Trans. Antennas Propag.* **2015**, *63*, 1234.
[19] T. Niu, W. Withayachumnankul, B. S.-Y. Ung, H. Menekse, M. Bhaskaran, S. Sriram, C. Fumeaux, *Opt. Express* **2013**, *21*, 2875.
[20] A. Tamminen, J. Ala-Laurinaho, S. Mäkelä, D. Gomes-Martins, J. Häkli, P. Koivisto, P. Rantakari, J. Säily, R. Tuovinen, A. R. Luukanen, M. Sipilä, A. V. Räisänen, *SPIE Defense Security Sensing* **2013**, *8715*, 871506.
[21] Y. Z. Cheng, W. Withayachumnankul, A. Upadhyay, D. Headland, Y. Nie, R. Z. Gong, M. Bhaskaran, S. Sriram, D. Abbott, *Appl. Phys. Lett.* **2014**, *105*, 181111.
[22] T. Niu, W. Withayachumnankul, A. Upadhyay, P. Gutruf, D. Abbott, M. Bhaskaran, S. Sriram, C. Fumeaux, *Opt. Express* **2014**, *22*, 16148.
[23] R. Singh, W. Cao, I. Al-Naib, L. Cong, W. Withayachumnankul, W. Zhang, *Appl. Phys. Lett.* **2014**, *105*, 171101.
[24] J. Ginn, B. Lail, J. Alda, G. Boreman, *Opt. Lett.* **2008**, *33*, 779.
[25] J. Lv, H. Liu, G. Si, *Micro Nano Lett.* **2015**, *10*, 5.
[26] G. Zheng, H. Mühlenbernd, M. Kenney, G. Li, T. Zentgraf, S. Zhang, *Nat. Nanotechnol.* **2015**, *10*, 308.
[27] D. Headland, P. Thurgood, D. Stavrevski, W. Withayachumnankul, D. Abbott, M. Bhaskaran, S. Sriram, *Opt. Mater. Express* **2015**, *5*, 1373.
[28] Z. H. Jiang, S. Yun, L. Lin, D. Brocker, D. H. Werner, T. S. Mayer, *Proc. IEEE Antennas Propag. Soc. Int. Symp.* **2012**.
[29] S. Liu, M. B. Sinclair, T. S. Mahony, Y. C. Jun, S. Campione, J. Ginn, D. A. Bender, J. R. Wendt, J. F. Ihlefeld, P. G. Clem, J. B. Wright, I. Brener, *Optica* **2014**, *1*, 250.
[30] C. Valagiannopoulos, A. Tukiainen, T. Aho, T. Niemi, M. Guina, S. Tretyakov, C. Simovski, *Phys. Rev. B* **2015**. *91*, 115305.
[31] R. Richtmyer, *J. Appl. Phys.* **1939**, *10*, 391.
[32] S. A. Long, M. W. McAllister, L. C. Shen, *IEEE Trans. Antennas Propag.* **1983**, *31*, 406.
[33] A. Petosa, A. Ittipiboon, *IEEE Antennas Propag. Mag.* **2010**, *52*, 91.
[34] L. Zou, W. Withayachumnankul, C. Shah, A. Mitchell, M. Klemm, M. Bhaskaran, S. Sriram, C. Fumeaux, *IEEE Photonics J.* **2014**, *6*, 4600110.
[35] L. Zou, W. Withayachumnankul, C. M. Shah, A. Mitchell, M. Bhaskaran, S. Sriram, C. Fumeaux, *Opt. Express* **2013**, *21*, 1344.
[36] K. Takano, Y. Yakiyama, K. Shibuya, K. Izumi, H. Miyazaki, Y. Jimba, F. Miyamaru, H. Kitahara, M. Hangyo, *IEEE Trans. Terahertz Sci. Technol.* **2013**, *3*, 812.
[37] J. Dai, J. Zhang, W. Zhang, D. Grischkowsky, *J. Opt. Soc. Am. B* **2004**, *21*, 1379.
[38] L. Cong, S. Tan, R. Yahiaoui, F. Yan, W. Zhang, R. Singh, *Appl. Phys. Lett.* **2015**, *106*, 031107.
[39] J. Hejase, P. R. Paladhi, P. P. Chahal, *IEEE Trans. Compon., Packag., Manuf., Technol.* **2011**, *1*, 1685.
[40] M. Ree, K.-J. Chen, D. Kirby, N. Katzenellenbogen, D. Grischkowsky, *J. Appl. Phys.* **1992**, *72*, 2014.
[41] I. Khodasevych, C. Shah, S. Sriram, M. Bhaskaran, W. Withayachumnankul, B. Ung, H. Lin, W. Rowe, D. Abbott, A. Mitchell, *Appl. Phys. Lett.* **2012**, *100*, 061101.
[42] M. Aznabet, M. Navarro-Cia, S. Kuznetsov, A. Gelfand, N. Fedorinina, Y. G. Goncharov, M. Beruete, O. El Mrabet, M. Sorolla, *Opt. Express* **2008**, *16*, 18312.
[43] H. Tao, A. Strikwerda, K. Fan, C. Bingham, W. Padilla, X. Zhang, R. Averitt, *J. Phys. D: Appl. Phys.* **2008**, *41*, 232004.
[44] D.-S. Kim, D.-H. Kim, S. Hwang, J.-H. Jang, *Opt. Express* **2012**, *20*, 13566.
[45] D.-H. Kim, D.-S. Kim, S. Hwang, J.-H. Jang, *Opt. Express* **2012**, *20*, 16815.
[46] S. Lee, S. Kim, T.-T. Kim, Y. Kim, M. Choi, S. H. Lee, J.-Y. Kim, B. Min, *Adv. Mater.* **2012**, *24*, 3491.
[47] J. Wang, S. Liu, S. Guruswamy, A. Nahata, *Appl. Phys. Lett.* **2013**, *103*, 221116.
[48] N. K. Grady, J. E. Heyes, D. R. Chowdhury, Y. Zeng, M. T. Reiten, A. K. Azad, A. J. Taylor, D. A. Dalvit, H.-T. Chen, *Science* **2013**, *340*, 1304.
[49] R. Ortuño, C. García-Meca, A. Martínez, *Plasmonics* **2014**, *9*, 1143.

[50] S. A. Kuznetsov, M. A. Astafev, M. Beruete, M. Navarro-Cía, *Sci. Rep.* **2015**, *5*, 7738.
[51] S. Liu, H. Chen, T. J. Cui, *Appl. Phys. Lett.* **2015**, *106*, 151601.
[52] F. Yang, P. Nayeri, A. Z. Elsherbeni, J. C. Ginn, D. J. Shelton, G. D. Boreman, Y. Rahmat-Samii, *IEEE Trans. Antennas Propag.* **2012**, *60*, 4202.
[53] W. Withayachumnankul, C. M. Shah, C. Fumeaux, K. Kaltenecker, M. Walther, B. M. Fischer, D. Abbott, M. Bhaskaran, S. Sriram, *Adv. Opt. Mater.* **2013**, *1*, 443.
[54] W. Withayachumnankul, C. M. Shah, C. Fumeaux, B. S.-Y. Ung, W. J. Padilla, M. Bhaskaran, D. Abbott, S. Sriram, *ACS Photonics* **2014**, *1*, 625.
[55] Y. Z. Cheng, W. Withayachumnankul, A. Upadhyay, D. Headland, Y. Nie, R. Z. Gong, M. Bhaskaran, S. Sriram, D. Abbott, *Adv. Opt. Mater.* **2015**, *3*, 376.
[56] M. R. Nikkhah, P. Loghmannia, J. Rashed-Mohassel, A. Kishk, *IEEE Trans. Antennas Propag.* **2014**, *62*, 3359.
[57] W. Withayachumnankul, B. M. Fischer, H. Lin, D. Abbott, *J. Opt. Soc. Am. B* **2008**, *25*, 1059.
[58] W. Withayachumnankul, J. F. O'Hara, W. Cao, I. Al-Naib, W. Zhang, *Opt. Express* **2014**, *22*, 972.
[59] S. Lucyszyn, *Piers Online* **2007**, *3*, 554.
[60] M. A. Ordal, L. L. Long, R. J. Bell, S. E. Bell, R. R. Bell, R. W. Alexander, C. A. Ward, *Appl. Opt.* **1983**, *22*, 1099.